

Article

Elasto-Inertial Particle Focusing in Microchannel with T-Shaped Cross-Section

Jaekyeong Jang ¹, Uihwan Kim ², Taehoon Kim ^{1,2,*} and Younghak Cho ^{1,2,*} 

¹ Department of Mechanical System Design Engineering, Seoul National University of Science & Technology, 232 Gongneung-ro, Nowon-gu, Seoul 01811, Korea

² Department of Mechanical Design and Robot Engineering, Seoul National University of Science & Technology, 232 Gongneung-ro, Nowon-gu, Seoul 01811, Korea

* Correspondence: tkim99@seoultech.ac.kr (T.K.); yhcho@seoultech.ac.kr (Y.C.); Tel.: +82-2-970-6340 (T.K.); +82-2-970-6361 (Y.C.)

Abstract: Recently, particle manipulation in non-Newtonian fluids has attracted increasing attention because of a good particle focusing toward the mid-plane of a channel. In this research, we proposed a simple and robust fabrication method to make a microchannel with various T-shaped cross-sections for particle focusing and separation in a viscoelastic solution. SU-8-based soft lithography was used to form three different types of microchannels with T-shaped cross-sections, which enabled self-alignment and plasma bonding between two PDMS molds. The effects of the flow rate and geometric shape of the cross-sections on particle focusing were evaluated in straight microchannels with T-shaped cross-sections. Moreover, by taking images from the top and side part of the channels, it was possible to confirm the position of the particles three-dimensionally. The effects of the corner angle of the channel and the aspect ratio of the height to width of the T shape on the elasto-inertial focusing phenomenon were evaluated and compared with each other using numerical simulation. Simulation results for the particle focusing agreed well with the experimental results both in qualitatively and quantitatively. Furthermore, the numerical study showed a potential implication for particle separation depending on its size when the aspect ratio of the T-shaped microchannel and the flow rate were appropriately leveraged.

Keywords: T-shaped cross-section; self-alignment; plasma bonding; elasto-inertial focusing; viscoelasticity



Citation: Jang, J.; Kim, U.; Kim, T.; Cho, Y. Elasto-Inertial Particle Focusing in Microchannel with T-Shaped Cross-Section. *Appl. Sci.* **2022**, *12*, 10552. <https://doi.org/10.3390/app122010552>

Academic Editor: Giuseppe Lazzara

Received: 28 September 2022

Accepted: 17 October 2022

Published: 19 October 2022

Publisher's Note: MDPI stays neutral with regard to jurisdictional claims in published maps and institutional affiliations.



Copyright: © 2022 by the authors. Licensee MDPI, Basel, Switzerland. This article is an open access article distributed under the terms and conditions of the Creative Commons Attribution (CC BY) license (<https://creativecommons.org/licenses/by/4.0/>).

1. Introduction

Microfluidic techniques for separating and manipulating particles or cells using various forces generated as fluid flows in a microchannel have been attracting increased attention over recent decades. These techniques can separate and manipulate particles without the use of external forces and are low-cost, have high processing efficiency and reduced sample consumption, and so have been used in various fields, such as medicine, chemistry and biology. Particle focusing and separation are important for preprocessing in biomedical analysis.

Viscoelastic microfluidics has been widely used to manipulate particles and cells using nonlinear elastic forces without any external force [1–4]. That is, particles can be focused and separated depending on their sizes in a viscoelastic fluid. Viscoelasticity causes elastic lift force on particles to drive them laterally to equilibrium positions, typically the center of the microchannel [5]. Compared with inertial focusing in a Newtonian fluid, true 3D particle focusing can be easily obtained in simple straight channels in a viscoelastic non-Newtonian fluid [6], due to the coupling of inertial effect and elastic effect (i.e., elasto-inertial focusing) [7–9]. Such elastic force results from an emergence of the first normal stress differences across the channel. Several studies on the first normal stress have been carried out to evaluate the effect of flow rate, channel geometry and corner angles on focusing patterns through numerical simulations and experiments [7,9–11]. Recently, it

was found that the elastic force increases at the obtuse corner of a channel cross-section, so that the particle focusing increases prominently. Raoufi et al. proposed a new complex straight channel to obtain a tighter focusing band for smaller particles and a wider range of flow rates than can be achieved with conventional straight channels [12]. The complex microchannels with a reflex angle in the corner of the channel cross-section were fabricated using micro-milling and micro-molding, and the behavior of particles in viscoelastic fluids was explored through experiments and simulations. It was shown that the corner angle of the cross-sectional shape of the microchannel influenced the particle focusing.

In general, microchannels can be easily fabricated using a polydimethylsiloxane (PDMS) replica molding process based on the classical soft-lithography technique, but their cross-sectional shapes are restricted to squares and rectangles due to the micro-mold shapes. Recently, microchannels with non-rectangular cross-sections, such as a circle, half-circle, triangle and trapezoid, have been presented [3,11,13,14]. In a previous study [15], we fabricated microchannels with various cross-sectional shapes, such as a parallelogram, rhombus, pentagon and hexagon. They were fabricated using basic micro-electro-mechanical systems (MEMS) processes, such as photolithography, reactive ion etching (RIE) and anisotropic potassium hydroxide (KOH) wet etching of Si followed by self-alignment between the Si channel and PDMS mold. However, it is not easy to fabricate microchannels with a reflex angle in the corner part of the channel cross-section using a conventional soft-lithography technique.

In the present work, we propose a novel yet simple fabrication method for a microchannel with a T-shaped cross-section, which is based on soft lithography, followed by self-alignment with two PDMS molds. We carried out experiments to confirm the elasto-inertial focusing position of particles for three kinds of microchannels with different sizes of T-shaped cross-sections in non-Newtonian fluid according to the flow rate and particle size. By taking images from the top and side parts of the microchannel, it was possible to confirm the position of the particles three-dimensionally. The effects of the corner angle of the channel as well as the aspect ratio of the height to width of the T-shaped microchannel on the elasto-inertial focusing phenomenon were evaluated and compared with each other using numerical simulation.

2. Materials and Methods

2.1. Fabrication of a Microchannel with a T-Shaped Cross-Section

In this research, we fabricated three kinds of microchannels with different T-shaped cross-sections. The fabrication method for microchannels with T-shaped cross-sections is briefly presented in Figure 1. The microchannels were simply formed using basic soft lithography as follows: (i) two kinds of SU-8 photoresists (SU-8 2050 and SU-8 2075, Kayaku Advanced Materials, Inc., Westborough, MA, USA) were spin-coated on Si wafers, and then patterned by UV lithography; (ii) two PDMS molds were made from two SU-8 master molds; (iii) self-alignment and O₂ plasma bonding between two PDMS molds were achieved. A small amount of DI water was sprayed between the two PDMS molds during self-alignment. Finally, the DI water was evaporated on a hotplate to complete the formation of the microchannels.

The details of the relationship between the width and height of two PDMS molds are shown in the inset of Figure 1. Table 1 shows the experimental conditions for SU-8 patterning for three kinds of microchannels with different T-shaped cross-sections and their dimensions.

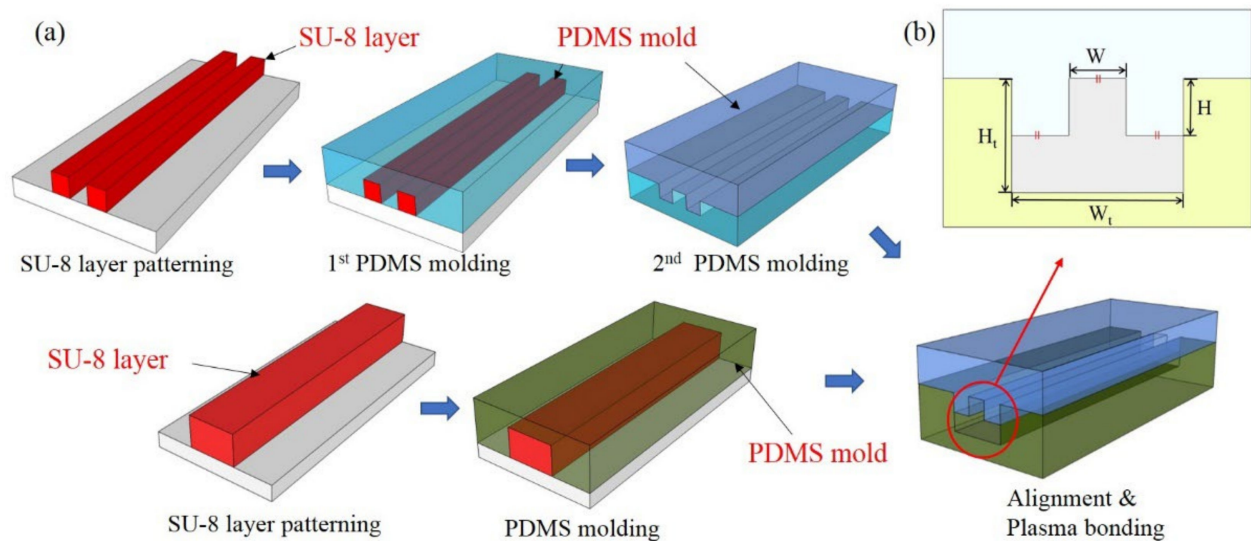


Figure 1. (a) Schematic 3D view of fabrication process; (b) design parameters between two PDMS molds (top and bottom) in microchannels with T-shaped cross-sections.

Table 1. Experimental conditions for SU-8 patterning and microchannel dimensions.

	Top Layer (W, H)			Bottom Layer (W_t, H_t)
	Type 1	Type 2	Type 3	
Photoresist	SU-8 2050	SU-8 2075	SU-8 2075	SU-8 2075
Coating speed (rpm)	3000	3000	2100	1300
Width (μm)	50	50	50	150
Height (μm)	35	52.5	70	105

2.2. Sample Preparation and Experimental Setup

In this research, PEO (polyethylene oxide) solution was used as the viscoelastic solution. To make 500 ppm PEO (PEO500) solution, PEO ($M_w = \sim 2$ MDa, Sigma-Aldrich, Burlington, MA, USA) was dissolved in DI water. Fluorescent polystyrene (PS) particles (Thermo Scientific Inc., Waltham, MA, USA) with 5 μm and 13 μm diameters were placed in the experimental solution (0.05–0.1 wt% concentration). To prevent particle aggregation during the particle focusing and separation experiments, Tween 20 (Sigma-Aldrich, Burlington, MA, USA) was added to the solution at 0.1 wt% as a surfactant. The estimated mean viscosity of the PEO500 solution was about 1.85 mPa·s (DI water: 0.89 mPa·s), and its relaxation time was estimated from the previous empirical relaxation time (λ_e), measured with a capillary breakup extensional rheometer (CaBER) [9,16]. The relaxation time for the PEO500 solution was estimated to be 3.78 ms on the basis of the empirical formula [9].

The particles in the microchannel with a T-shaped cross-section were observed using optical microscopes (BX-60, Olympus, Tokyo, Japan). The flow rates were controlled from 1 to 150 $\mu\text{L}/\text{min}$ with a syringe pump (LEGATO 111, KD Scientific Inc., Holliston, MA, USA), and the focusing positions of the particles were recorded and captured at 1 cm, 4 cm and 7 cm downstream from the inlet using a CMOS camera (ZWO Co., Ltd., Suzhou, China). For the precise analysis of the particle focusing behavior, bright-field and fluorescent images were captured from the top and side of the microchannel with exposure times of 20 ms and 500 ms. All the analyses and postprocessing of the images were achieved using the open-source ImageJ software. In this research, the fluorescent intensity profiles across the microchannel were obtained and fitted with a Gaussian distribution.

2.3. Simulation for Viscoelastic Flow

The current simulation aimed to explore the influence of T-shaped cross-sections with varying aspect ratios (i.e., H/W) on elasto-inertial particle migration, mainly when the particle was suspended in a viscoelastic fluid. This numerical study was designed to corroborate the results of the experimental study and thus provide an underlying mechanism for particle migration. To this end, we used a finite-volume-based flow solver (ANSYS Fluent) to assess the equilibrium position of the inertial particles, where all the forces acting upon the particles balance each other in the microchannel. In this numerical study, we utilized two types of channels (i.e., Type 2 and Type 3), with an aspect ratio (i.e., H/W see Figure 2) of 1 and 1.4, respectively. Each microchannel had an axial length of 1 mm to ensure a fully developed condition at the downstream measurement location. The physical dimensions of each channel cross-section are shown in Table 1, and they were kept identical to those used in the experimental works for an appropriate comparison. The x origin resided on the symmetric plane for both cross-sections. In contrast, the y origin was at the half-height of the bottom channel, corresponding to $25\ \mu\text{m}$ and $15\ \mu\text{m}$ away from the bottom wall for Type 2 and Type 3, respectively. Note that the Type 2 channel was considered as a baseline for comparison since it had an aspect ratio of unity. Due to the larger aspect ratio, the Type 3 channel was characterized by a shallow channel depth (i.e., $30\ \mu\text{m}$) and a long neck (i.e., $70\ \mu\text{m}$). Thus, a coupled effect between the bottom wall and the sharp edge at the junction could be promoted as compared to the case of the Type 2 channel. Furthermore, it should be noted that the vertical length for both Type 2 and Type 3 channels was slightly shorter than those used in the present experiment. We intentionally used this shorter length to keep the H/W as 1 and 1.4 for each microchannel. Nonetheless, the difference in D_h between the numerical and experimental studies was less than 5% for all cases and was thus negligible.

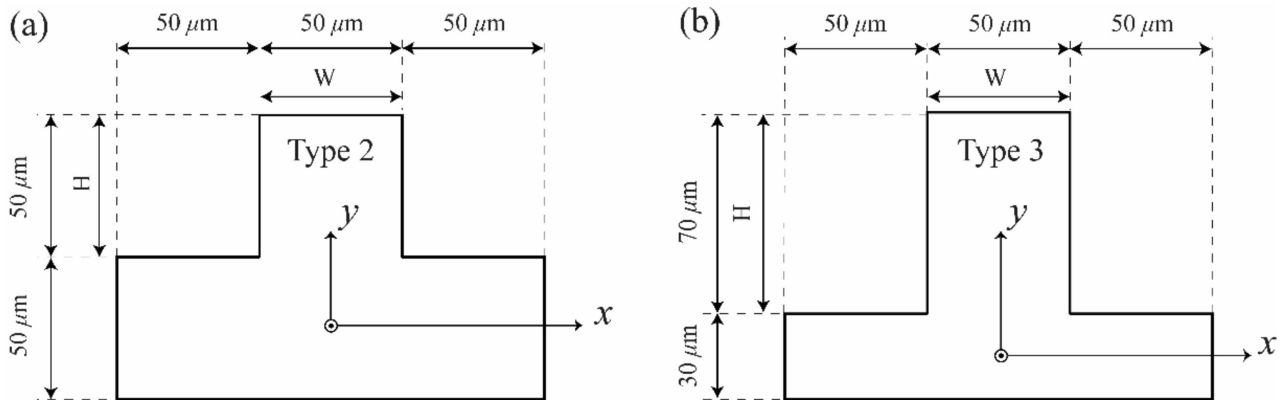


Figure 2. Cross-sectional shape and dimensions of (a) Type 2 and (b) Type 3 microchannel considered in the numerical simulation. x and y on a cross-plane represent a horizontal and a vertical axis in the Cartesian coordinate system considered in the numerical simulation.

In this numerical study, uniform velocity and pressure were applied for each inlet and outlet. Four selective flow rates (i.e., 1, 10, 100 and $150\ \mu\text{L}/\text{min}$) were used, corresponding to the centerline velocity, U_{max} , in a range of 0.0037 – $0.59\ \text{m/s}$. Flow parameters and the resulting channel Reynolds number ($Re = \rho U_{max} D_h / \mu$, where ρ is the fluid density, U_{max} is the characteristic velocity, D_h is the hydraulic diameter of the current microchannels, μ is the mean viscosity, respectively) are summarized in Table 2. Two particle diameters (i.e., $d = 5$ and $13\ \mu\text{m}$) were considered similar to the experiments. The particle Reynolds number ($Re_p = Re (d/D_h)^2$, where d is the particle diameter) was thus in a range of $O(10^{-2})$ – $O(10^0)$. The exact value of the particle parameters in this numerical study are also reported in Table 2.

Table 2. Flow and particle parameters in the numerical simulation.

Case	Cross-Section	d (μm)	Flow Rate ($\mu\text{L}/\text{min}$)	U_{max} (m/s)	Re	Re_p
T ₂ D5Q1	Type 2	5	1	0.0037	0.29	1.84×10^{-2}
T ₂ D5Q10	Type 2	5	10	0.037	2.90	1.84×10^{-1}
T ₂ D5Q100	Type 2	5	100	0.37	29.0	1.84×10^0
T ₂ D13Q1	Type 2	13	1	0.0037	0.29	4.79×10^{-2}
T ₂ D13Q10	Type 2	13	10	0.037	2.90	4.79×10^{-1}
T ₂ D13Q100	Type 2	13	100	0.37	29.0	4.79×10^0
T ₃ D5Q1	Type 3	5	1	0.0038	0.24	1.84×10^{-2}
T ₃ D5Q10	Type 3	5	10	0.038	2.42	1.84×10^{-1}
T ₃ D5Q100	Type 3	5	100	0.38	24.2	1.84×10^0
T ₃ D5Q150	Type 3	5	150	0.59	37.6	2.94×10^0
T ₃ D13Q1	Type 3	13	1	0.0038	0.24	1.84×10^{-2}
T ₃ D13Q10	Type 3	13	10	0.038	2.42	1.84×10^{-1}
T ₃ D13Q100	Type 3	13	100	0.38	24.2	1.84×10^0
T ₃ D13Q150	Type 3	13	150	0.59	37.6	2.94×10^0

A single, rigid, spherical particle was set at a fixed location on the cross-plane for both the Type 2 and Type 3 channels. Then, a net lift force acting on the particles was computed, varying with the particle location along the horizontal and vertical axis as depicted in Figure 2. Since the viscoelastic effect on the inertial particle was of particular interest in this study, we simulated the viscoelastic fluid by leveraging the user-defined function (UDF) provided by the software package. This UDF allowed us to model the viscosity of the current working fluid (i.e., PEO500 solution) depending on a range of shear rates. Based on the measured data of the viscosity varying with the shear rate [17], a power-law model was specified and successfully applied to our simulation study, as was applied in our previous works [9,18]. It should be noted that the flow rate greater than 100 $\mu\text{L}/\text{min}$ considered herein caused a shear rate ($\dot{\gamma}$) that exceeded the measured range of the shear rate reported by [9]. However, Lim et al. [17] showed that the viscoelastic effect of the PEO500 solution becomes negligible when the shear rate is greater than 100 (1/s) as its viscosity becomes constant at 1 mPa·s. Therefore, the lower boundary of the present power-law model was set to the one when $\dot{\gamma} \geq 1000$. In this simulation, an unstructured non-uniform grid was employed to discretize the entire computational domain, and the total number of grid points was approximately 500,000 in all cases. In particular, the grid resolution around the spherical particle was set to $\Delta/d = 0.1$ (where Δ is the grid resolution) for both particle sizes (5 μm and 13 μm) for consistency.

3. Results and Discussion

The elasto-inertial particle focusing in viscoelastic non-Newtonian fluid flowing through a straight microchannel is a result of competition between the inertial lift force and elastic force [6]. It has also been clarified that the channel cross-section plays an essential role in particle focusing. When flowing through a straight microchannel, initially random suspensions of particles reach certain equilibrium positions.

The Reynolds number (Re) is defined as $Re = \rho U_{max} D_h / \mu$ (ρ is the fluid density, U_{max} is the characteristic velocity, D_h is the hydraulic diameter, μ is the mean viscosity), which is used to quantify the relative importance of the inertial and viscous effect for a given flow condition. A dimensionless Weissenberg number (Wi) is defined as $Wi = \lambda \dot{\gamma} = 2 \lambda U_{max} / D_h$ (λ is the relaxation time of the polymer solution, $\dot{\gamma}$ is the shear rate), which is used to quantify the viscoelastic effects of a fluid and describes the ratio of elastic and viscous forces. To compare the relative importance of the elastic effect to the inertial effect, the fluid elasticity (El) is defined as the ratio of the Weissenberg number to the Reynolds number,

i.e., $El = Wi/Re = 2 \lambda \mu / (\rho D_h^2)$ [19], which is a dimensionless number and can determine the number of particle focusing points under a non-Newtonian viscoelastic fluid.

Figure 3 shows the SEM (scanning electron microscope) images of three kinds of microchannels with different T-shaped cross-sections. They show that the two PDMS molds were perfectly aligned and bonded thanks to their geometrical shapes, as shown in Figure 1. The detailed dimensions of the fabricated microchannels are listed in Table 1.

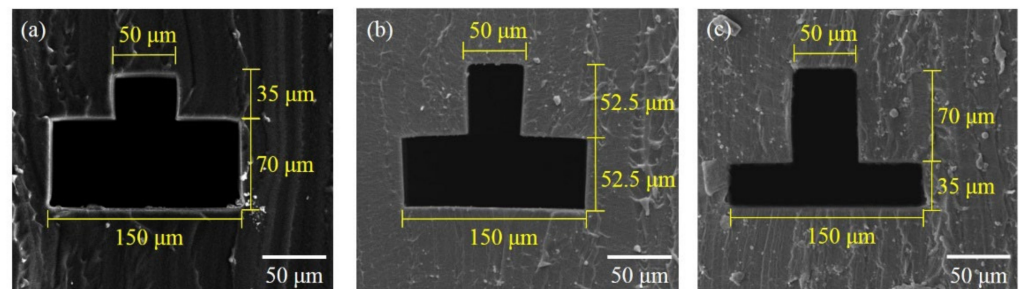


Figure 3. SEM images of microchannels with a T-shaped cross-section. (a) Type 1, (b) Type 2, (c) Type 3.

3.1. Viscoelastic Particle Focusing under Non-Newtonian Fluid

First, we investigated and observed the focusing and migration of particles under a viscoelastic fluid in three kinds of microchannels with different T-shaped cross-sections. Furthermore, experiments were carried out for two sizes of particles (5 and 13 μm diameter), which is one of the important parameters for determining elasto-inertial particle focusing behaviors [20].

Figure 4 shows the particle focusing at a flow rate of 100 $\mu\text{L}/\text{min}$ according to the location from the inlet of the Type 3 microchannel in non-Newtonian viscoelastic fluid (PEO500). At the location near the inlet (1 cm), no focusing was observed for either particle size due to the insufficient elastic forces developed. As the channel length was increased to 7 cm, particles were focused in a single stream located at the center, with a flow rate of 100 $\mu\text{L}/\text{min}$. The lateral migration speed was strongly dependent upon particle size [21,22], so tighter particle focusing was obtained for the 13 μm particle 7 cm downstream from the inlet.

Figure 5 presents the optical images of particle focusing (top and side view) in the microchannel with different T-shaped cross-sections for different flow rates and particle sizes in non-Newtonian viscoelastic fluid. All optical images were captured 7 cm downstream. The dotted lines are the boundaries of the microchannel from the top and side view, which were obtained from the bright-field optical images. Figure 6 presents the normalized fluorescent intensity profiles presenting the particle distribution at various flow rates in the microchannel with different T-shaped cross-sections including a microchannel with a square cross-section which was prepared for comparison.

As shown in Figure 5a,c,e, when viewed from the side, 13 μm particles were observed to focus to a single line near the bottom side for all types of channels. Furthermore, the effect of elasto-inertial force was dominant for low flow rates ((below 50 $\mu\text{L}/\text{min}$, $Re \approx 0$ and $Wi > 0$) so the particles moved to the centerline for all types of channels (top view). The experimental results show that there was only one stream from both front and side views, meaning that true 3D elasto-inertial particle focusing was achieved for the tested condition. On the other hand, when the flow rate increased and reached 50 $\mu\text{L}/\text{min}$ ($Re > 0$ and $Wi > 0$), the single-line particle focusing changed to double-line focusing in the Type 1 channel, but there was no change in the Type 2 and Type 3 channels. For the higher flow rate of 100 $\mu\text{L}/\text{min}$ (inertial force dominant regime), due to the relatively strong inertial force at the high flow rate [6], the focused particles were more or less dispersed around the centerline in the Type 2 channel and the triple-line focusing was observed in the Type 3 channel. This implies that the lateral migration of particles in a non-Newtonian fluid is strongly affected by the inertial force rather than the elastic force [20].

As shown in Figure 5b,d,f, particles with a relatively small particle size ($5\ \mu\text{m}$) were randomly dispersed and not focused at specific points in the Type 1 and Type 2 channels for low flow rates (below $50\ \mu\text{L}/\text{min}$, $Re \approx 0$ and $Wi > 0$). In the case of the Type 3 channel, however, small particles were slightly focused in the centerline for low flow rates. As the flow rate increased up to $50\ \mu\text{L}/\text{min}$ ($Re > 0$ and $Wi > 0$), the particles were focused in the center of the microchannels under the influence of elasto-inertial force. However, unlike the large particles ($13\ \mu\text{m}$), the small particles were not completely focused in the center, showing wider focused bands. This was due to the competition between the non-negligible inertial lift force and the relevant elastic force under viscoelastic fluid flowing [6,20].

Consequently, the particle migration and focusing were more distinct for large particles because the force on the particle induced by the normal stress was proportional to the cube of the particle diameter [20]. In the cases of the Type 1 and Type 2 channels, tighter focusing was generally observed for the large particles such as the square channel, but the small particles were rather tightly focused in the center of the channel at high flow rates (over $100\ \mu\text{L}/\text{min}$) in the Type 3 channel. Moreover, the Type 3 channel showed a peculiar phenomenon in which large particles did not gather but moved to special focusing points. In total, there were three focusing points.

Figure 7 shows the positions of $5\ \mu\text{m}$ and $13\ \mu\text{m}$ particles distributed within the channel at the flow rate of $100\ \mu\text{L}/\text{min}$ for three types of channels. As the aspect ratio increased (from Type 1 to Type 3), small particles were more tightly focused in the center. However, there was not enough force acting on the large particles in the side part of the channel to move them to the center, and they were focused in the side part of the channel. This will be explained in the section reporting the simulation.

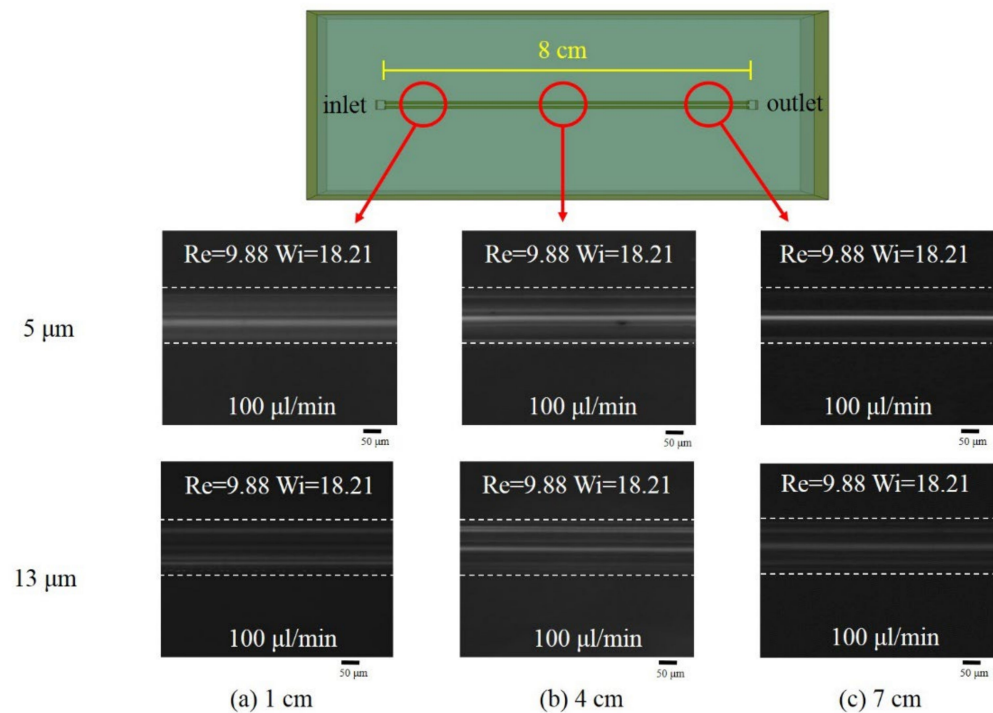
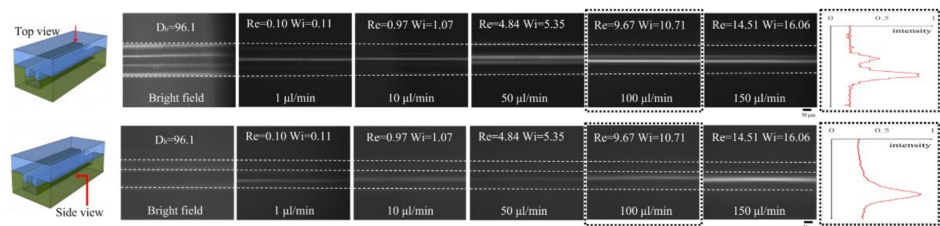
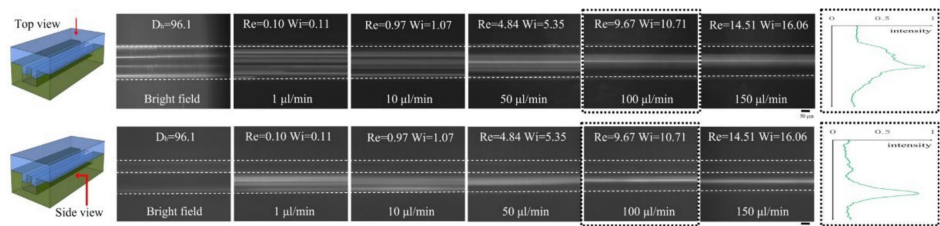


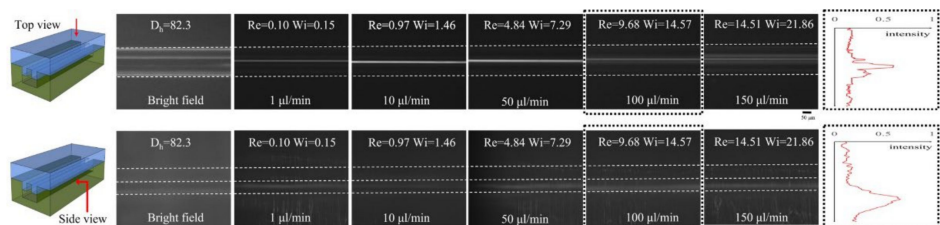
Figure 4. Optical images (top view) at a $100\ \mu\text{L}/\text{min}$ flow rate in viscoelastic fluid at different distances from the inlet for different particle sizes. (a) 1 cm, (b) 4 cm, (c) 7 cm from the inlet of the Type 3 channel.



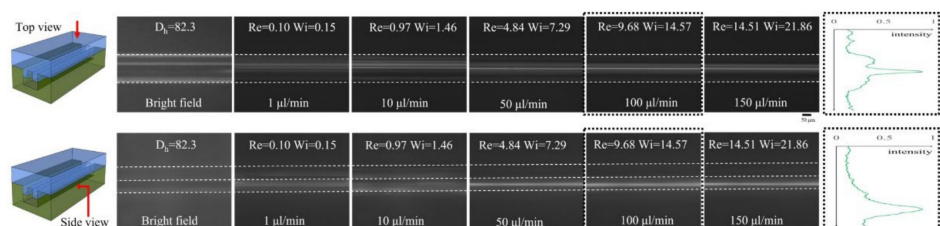
(a) Results for 13 μm particle for Type 1 channel.



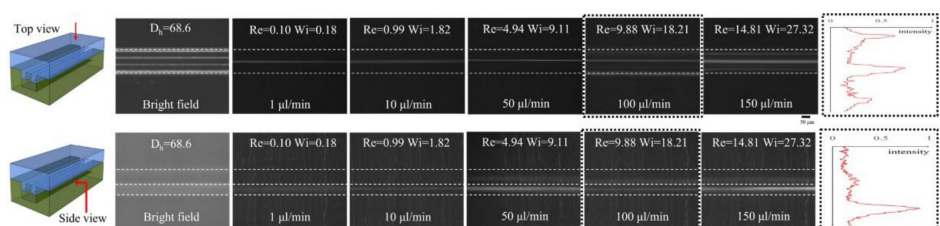
(b) Results for 5 μm particle for Type 1 channel.



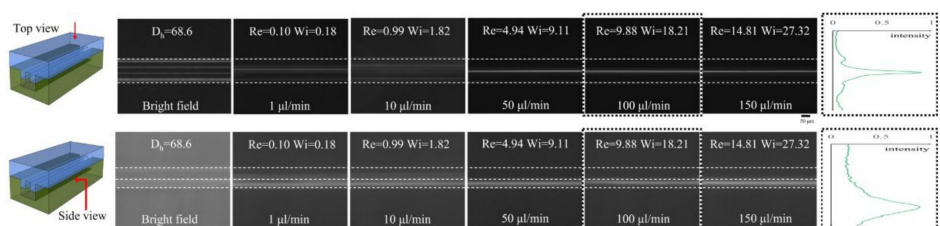
(c) Results for 13 μm particle for Type 2 channel.



(d) Results for 5 μm particle for Type 2 channel.



(e) Results for 13 μm particle for Type 3 channel.



(f) Results for 5 μm particle for Type 3 channel.

Figure 5. Optical images and intensity graphs (top and side view) of particle focusing under viscoelastic fluid according to various flow rates for three types of channels.

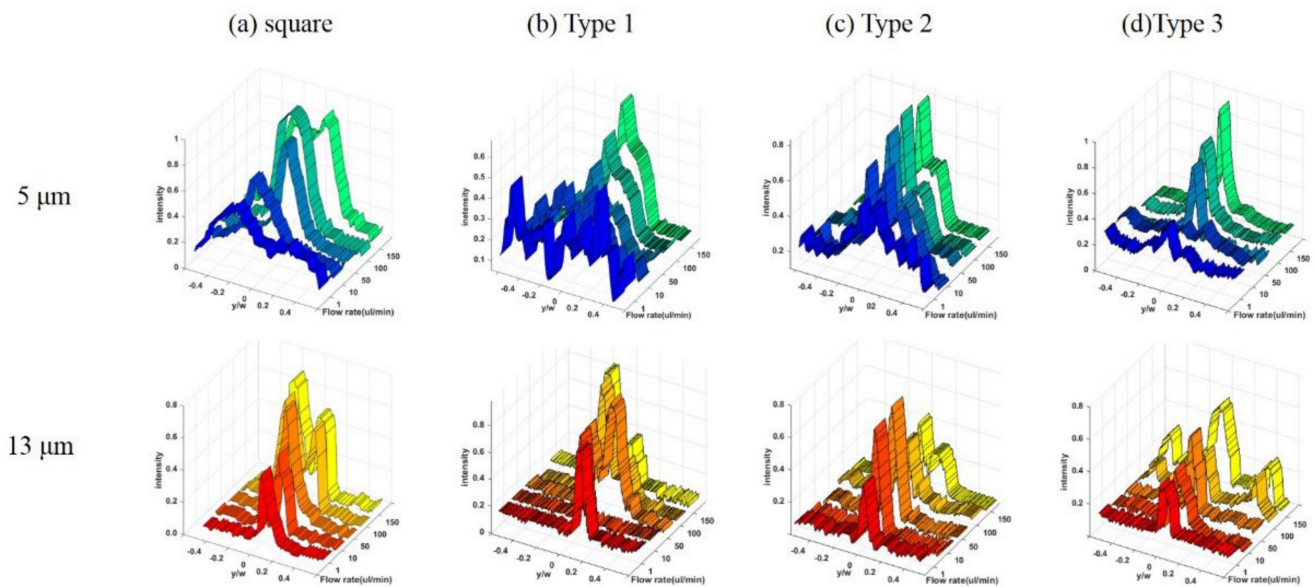


Figure 6. Fluorescence intensity under viscoelastic fluid (top view) for 5 μm and 13 μm particles in (a) square channel, (b) Type 1 channel, (c) Type 2 channel and (d) Type 3 channel.

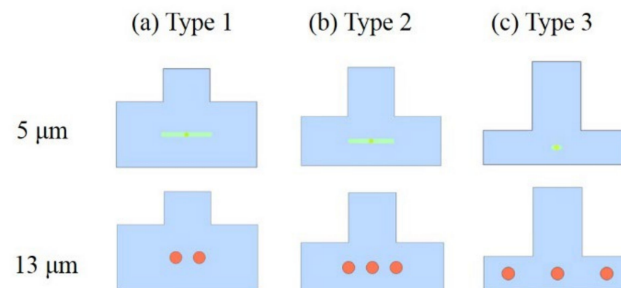


Figure 7. Positions of 5 μm and 13 μm particles distributed within the channel for the flow rate of 100 $\mu\text{L}/\text{min}$. (a) Type 1 channel, (b) Type 2 channel and (c) Type 3 channel.

3.2. Simulation Results

In order to first assess the flow pattern without the inertial particle on the channel cross-plane, Figure 8a,b show contour maps of the axial velocity (U) at the flow rate of 10 $\mu\text{L}/\text{min}$ as a representative case for Type 2 and Type 3, respectively. The axial velocity was normalized by its maximum (U_{max}), while we used an actual physical unit for both the horizontal and vertical axis. Figure 8 shows that the aspect ratio of the channel significantly affects the mean flow structure on the cross-plane. For example, the horizontal location of U_{max} for both Type 2 and Type 3 is the same, residing on the symmetric plane (i.e., $x = 0$). However, the vertical location of U_{max} is different depending on the aspect ratio of the channel cross-section. For Type 2, the local maximum in U occurs below the junction (i.e., $y = 10 \mu\text{m}$), whereas Type 3 has a local maximum above the junction on the vertical axis (i.e., $y = 25 \mu\text{m}$). This is because the shallow bottom channel for Type 3 induces a higher-pressure zone that moves the location of U_{max} further away from the bottom wall. Furthermore, the presence of the higher-pressure zone for Type 3 affects the mean flow topology, as shown in Figure 8a,b. Since $H/W = 1$ for Type 2, most of the fluid travels through the bottom channel, while the fluid in Type 3 mainly goes through the upper channel.

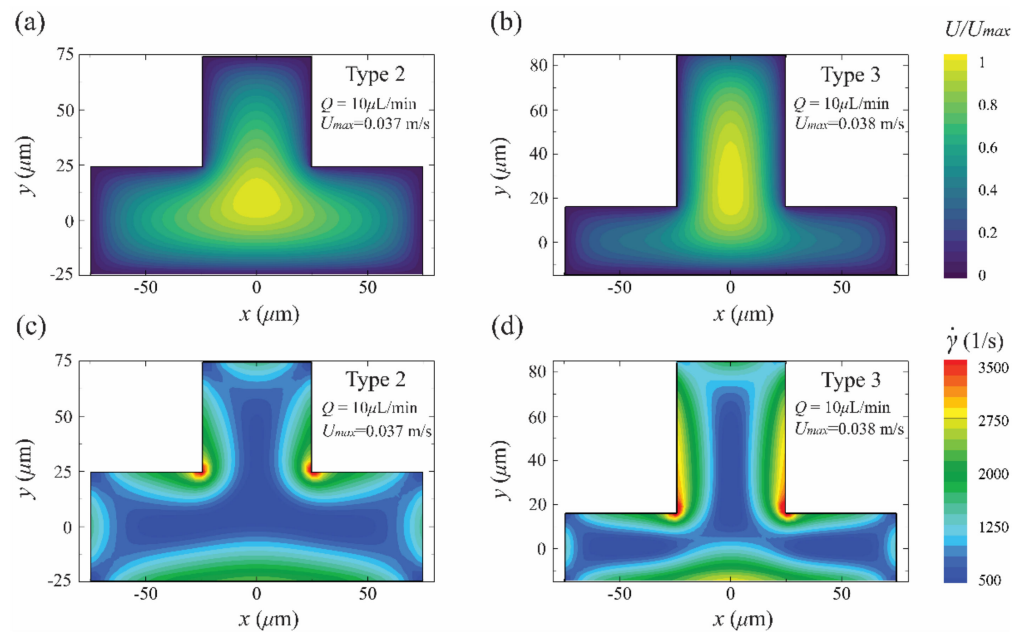


Figure 8. Simulation results of the (a,b) axial velocity magnitude U , normalized by the maximum axial velocity U_{max} , for Type 2 and Type 3 channels, and (c,d) shear rate, $\dot{\gamma}$ for each Type 2 and Type 3 channels at the flow rate of 10 $\mu\text{L}/\text{min}$.

The contour maps of the shear rate for both channels are presented in Figure 8c,d. As reported in the previous study [23], the shear rate as a differential of the fluid velocity plays a crucial role in particle migration in the viscoelastic regime. This is because the shear rate is closely correlated with the competing mechanism of the inertial lift force between the shear gradient and wall interaction. Furthermore, previous studies [7,23] have shown a preferential migrating pattern of the inertial particles toward the region where the shear rate is zero, particularly when the second normal stress difference in a viscoelastic fluid is negligible. With these notions, Figure 8c,d give a qualitative picture of the migration pattern of the elasto-inertial particles for the cross-section shapes considered in this study. It is clear that each wall created a relatively higher shear rate, whereas the center and each corner of the channel cross-section had the lowest shear rate for both Type 2 and Type 3, as observed in the previous studies [3,11,20]. Most importantly, the protruding sharp edges at the junction caused the highest shear rate for both channels. The effect of these sharp edges became more significant when they were coupled with the bottom wall effect as the aspect ratio increased (see Figure 8d). For example, the topology of the low shear rate (i.e., $\dot{\gamma} < 1000 \text{ s}^{-1}$) seems bottleneck-like for Type 3. Based on these observations, it can be expected that the migrating pattern of the elasto-inertial particles passing through the Type 3 channel would be different to those in the Type 2 channel.

Figure 9 presents the variation in x- and y-directional net elasto-inertial force (F_{net}) for 5 and 13 μm particles in the Type 2 channel along the aforementioned lines, as illustrated in Figure 2. The normalization was made for F_{net} by $\rho_f U_{max}^2 d^4/D_h^2$, where ρ_f and U_{max} denote the fluid density and the maximum velocity of the channel. As mentioned earlier, the horizontal axis in Figure 9 used an actual physical unit, which is better for describing the particle location with respect to the origin. Symbols for each case are denoted in the legend in Figure 9. Solid lines connecting through the data points were made by piecewise cubic interpolation to show a shape-preserving trend in F_{net} along the x and y axis. Note that the current simulation could not resolve a valid F_{net} after a certain point when the spherical particle resided in the proximity of the channel wall. It should also be noted that the negative value in F_{net} when x (or y) > 0 represents a directional force toward the origin, while its positive value when x (or y) < 0 indicates a directional force toward the wall.

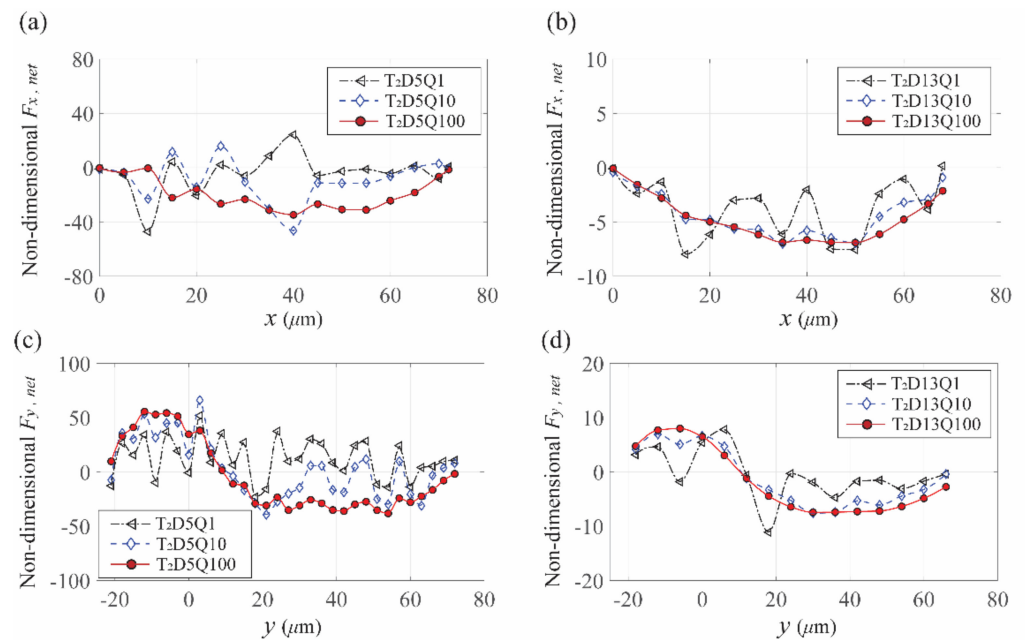


Figure 9. Variation in (a,b) x-directional and (c,d) y-directional net elasto-inertial force exerted on 5 and 13 μm particles suspended in the Type 2 channel. Measurements were made for various particle locations along the x and y axis illustrated in Figure 2.

For both the 5 and 13 μm particles shown in Figure 9a,b, $F_{x,net}$ is always negative and has a single zero crossing at the origin at a flow rate of 100 $\mu\text{L}/\text{min}$ for Type 2 (i.e., T₂D5Q100, T₂D13Q100, red symbols). This indicates that both 5 and 13 μm particles suspended in a viscoelastic fluid are likely to drift toward the origin in a lateral direction when the fluid inertia is sufficient. This numerical observation agrees well with our experiments, showing a single train of particles for both sizes at the same flow rate, as shown in Figure 5c,d. However, at the lower flow rate (i.e., 1 and 10 $\mu\text{L}/\text{min}$) in Figure 9a,b, a different pattern in $F_{x,net}$ between two inertial particles can be observed. For example, $F_{x,net}$ for the larger particle (i.e., 13 μm) still shows a negative with a single equilibrium point at the origin despite some fluctuations in $F_{x,net}$ at the lowest flow rate (i.e., 1 $\mu\text{L}/\text{min}$). This means the lateral drift consistently occurred for large particles (13 μm) independent of the flow rate within our measured range. For the case of small particles (5 μm), on the other hand, $F_{x,net}$ has multiples of zero crossings at the lower flow rates, as shown in Figure 9a, indicating wide dispersion of inertial particles along the lateral direction. These numerical results confirm a unique migrating behavior of the inertial particles depending on the particle size and the flow rate reported in our experiments (see Figure 5d).

Similar drifting patterns of elasto-inertial particles can also be observed for the vertical direction in Figure 9c,d. For the large particle size (i.e., 13 μm), the equilibrium point in $F_{y,net}$ is made independent of the current flow rates and consistently resides at 10 μm away from the vertical origin for all cases (see Figure 9d). The case of the small particle also shows a similar trend in $F_{y,net}$ and an equilibrium point at the highest flow rate, as shown in Figure 9c. This observation in our numerical study explains the particle focusing when the effect of the elasto-inertial force is large enough due to either a high degree of the flow rate or a large particle surface area. Furthermore, the vertical equilibrium point observed herein is where the local minimum $\dot{\gamma}$ and the local maximum U are positioned.

In this study, our experimental result shows a different migrating pattern of particles depending on their size, particularly in the Type 3 channel, and thus has a potential implication for particle separation by leveraging the aspect ratio of the current T-shaped channel. Therefore, in this numerical study, it is of particular importance to confirm such migrating behavior can be observed in the Type 3 channel and explore their background mechanism compared to the one in the Type 2 channel. Note that the x -directional net

forces are only considered in this case since y-directional net forces for Type 3 have the same trend and equilibrium point as those of Type 2. It should also be noted that the maximum flow rate increases at 150 $\mu\text{L}/\text{min}$ as the characteristic drift for the larger particles started to occur at the flow rate of 150 $\mu\text{L}/\text{min}$ in the present experiment.

Figure 10 shows the variation in the x-directional net force exerted on two different particles varying with the flow rates. For the case of the 5 μm particle, the first two lowest flow rates (i.e., T₃D5Q1 and T₃D5Q10) generate multiples of the zero crossing in the x-directional force, indicating an absence of the particle focusing in the lateral direction, as shown in Figure 10a. With an increase in flow rate, however, a consistent directional force occurs and pushes the 5 μm particle toward the origin of Type 3, indicating a single train of the particle focusing along the lateral centerline from 100 $\mu\text{L}/\text{min}$. These migrating patterns for the smaller particle agreed well with the results of the experiment, as seen in Figure 5f. The case of 13 μm particle, however, shows unique migrating behavior as the flow rate increases. When increasing the flow rate up to 100 $\mu\text{L}/\text{min}$, as shown in Figure 10b, $F_{x,net}$ becomes more consistent, moving the particle toward the lateral origin with a single equilibrium point. This is supported by our experimental observations, shown in Figure 5e, that the intensity of the fluorescent particles focused at the lateral centerline becomes higher, up to a flow rate of 100 $\mu\text{L}/\text{min}$. Interestingly, at the flow rate of 150 $\mu\text{L}/\text{min}$, the migrating pattern in the lateral direction for 13 μm particle case remarkably changes in the Type 3 channel. As shown in Figure 10b, $F_{x,net}$ at the maximum flow rate is characterized by two negative convexes and a positive plateau between them. This indicates two possible points of the particle focusing each at $x = 0$ and $x = 55 \mu\text{m}$, which is not observed in the case of 5 μm particles at the same flow rate. The interesting pattern of the particle focusing in Type 3 depending on the particle size could be attributed to the coupled effect between the sharp edge at the junction and the bottom wall (see Figure 8d). As was discussed earlier, the shallow channel depth with a protruded sharp edge as in Type 3 resonates with the effect of the shear rate on its cross-plane. Thus, the Type 3 channel preferentially segregates the large particle (i.e., 13 μm) with two lateral locations for the particle focusing. In contrast, the small particle (i.e., 5 μm) consistently drifts toward a single focusing point at the lateral origin at a flow rate of 150 $\mu\text{L}/\text{min}$. This numerical result has excellent agreement with our experimental result at the same flow rate in the same microchannel. Furthermore, the current observation suggests a potential implication of the particle separation depending on its size when the aspect ratio of the T-shaped microchannel and the flow rate are appropriately leveraged.

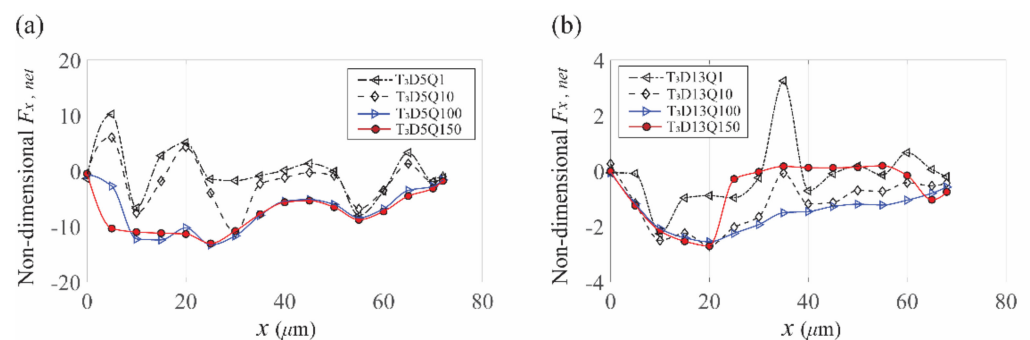


Figure 10. Variation in x-directional net elasto-inertial force exerted on (a) 5 μm and (b) 13 μm particles suspended in the Type 3 channel. Measurements were made for various particle locations along the x axis illustrated in Figure 2.

4. Conclusions

In this work, three kinds of PDMS microchannels with different T-shaped cross-sections were fabricated using SU-8 patterning, micro-molding and self-alignment of PDMS molds. For three kinds of microchannels with different sizes of T-shaped cross-sections, the elasto-inertial particle focusing behaviors in non-Newtonian fluids were investigated

according to the flow rate and particle size as well as the position of the channel downstream from inlet. From the images from the top and side part of the microchannels, it was possible to confirm the position of the particles three-dimensionally. The effects of the corner angle of the channel as well as the ratio of the top channel to the bottom channel of the T-shaped microchannel on the elasto-inertial focusing phenomenon were evaluated and compared with each other using a numerical simulation. The numerical studies showed the coupled effect of cross-sectional geometry and viscoelasticity on the particle migration pattern. Numerical results for the particle focusing agreed well with the experimental results both in qualitatively and quantitatively. As a final comment, our observation both in the experimental and numerical studies showed a potential implication for particle separation depending on its size when the aspect ratio of the T-shaped microchannel and the flow rate are appropriately leveraged. Specifically, the higher shear rate induced by a sharp edge at the T junction and its close proximity to the bottom wall may play a crucial role as a filter in particle separation. Therefore, our results suggest that two different sizes of particles (i.e., 5 and 13 μm in this study) can be effectively separated if the Type 3 channel is adapted together with the sheath flow.

Author Contributions: Conceptualization, Y.C.; methodology, Y.C.; software, T.K.; validation, J.J. and U.K.; formal analysis, J.J.; investigation, J.J. and U.K.; resources, Y.C.; data curation, J.J.; writing—original draft preparation, Y.C.; writing—review and editing, Y.C. and T.K.; visualization, J.J.; supervision, Y.C. and T.K.; project administration, Y.C.; funding acquisition, Y.C. All authors have read and agreed to the published version of the manuscript.

Funding: This work was supported by the National Research Foundation of Korea (NRF) grant funded by the Korean government (No. NRF-2020R1F1A1050178). Furthermore, it was partially supported by the Korea Institute for Advancement of Technology (KIAT) grant funded by the Korea Government (MOTIE). (P0012744, The Competency Development Program for Industry Specialist).

Institutional Review Board Statement: Not applicable.

Informed Consent Statement: Not applicable.

Data Availability Statement: Not applicable.

Conflicts of Interest: The authors declare no conflict of interest.

References

1. Nam, J.; Jang, W.S.; Lim, C.S. Non-electrical powered continuous cell concentration for enumeration of residual white blood cells in WBC-depleted blood using a viscoelastic fluid. *Talanta* **2019**, *197*, 12–19. [[CrossRef](#)]
2. Nam, J.; Namgung, B.; Lim, C.T.; Bae, J.-E.; Leo, H.L.; Cho, K.S.; Kim, S. Microfluidic device for sheathless particle focusing and separation using a viscoelastic fluid. *J. Chromatogr. A* **2015**, *1406*, 244–250. [[CrossRef](#)]
3. Kim, J.; Lee, J.; Wu, C.; Nam, S.; Di Carlo, D.; Lee, W. Inertial focusing in non-rectangular cross-section microchannels and manipulation of accessible focusing positions. *Lab Chip* **2016**, *16*, 992–1001. [[CrossRef](#)]
4. Tian, F.; Zhang, W.; Cai, L.; Li, S.; Hu, G.; Cong, Y.; Liu, C.; Li, T.; Sun, J. Microfluidic co-flow of Newtonian and viscoelastic fluids for high-resolution separation of microparticles. *Lab Chip* **2017**, *17*, 3078–3085. [[CrossRef](#)]
5. Kwon, T.; Choi, K.; Han, J. Separation of Ultra-High-Density Cell Suspension via Elasto-Inertial Microfluidics. *Small* **2021**, *17*, 2101880. [[CrossRef](#)]
6. Yang, S.; Kim, J.Y.; Lee, S.J.; Lee, S.S.; Kim, J.M. Sheathless elasto-inertial particle focusing and continuous separation in a straight rectangular microchannel. *Lab Chip* **2010**, *11*, 266–273. [[CrossRef](#)]
7. Yuan, D.; Zhao, Q.; Yan, S.; Tang, S.-Y.; Alici, G.; Zhang, J.; Li, W. Recent progress of particle migration in viscoelastic fluids. *Lab Chip* **2018**, *18*, 551–567. [[CrossRef](#)]
8. Zhou, J.; Papautsky, I. Viscoelastic microfluidics: Progress and challenges. *Microsyst. Nanoeng.* **2020**, *6*, 113. [[CrossRef](#)]
9. Kim, U.; Kwon, J.-Y.; Kim, T.; Cho, Y. Particle Focusing in a Straight Microchannel with Non-Rectangular Cross-Section. *Micromachines* **2022**, *13*, 151. [[CrossRef](#)]
10. Liu, C.; Xue, C.; Chen, X.; Shan, L.; Tian, Y.; Hu, G. Size-Based Separation of Particles and Cells Utilizing Viscoelastic Effects in Straight Microchannels. *Anal. Chem.* **2015**, *87*, 6041–6048. [[CrossRef](#)]
11. Tang, W.; Fan, N.; Yang, J.; Li, Z.; Zhu, L.; Jiang, D.; Shi, J.; Xiang, N. Elasto-inertial particle focusing in 3D-printed microchannels with unconventional cross sections. *Microfluid. Nanofluid.* **2019**, *23*, 42. [[CrossRef](#)]
12. Raoufi, M.A.; Mashhadian, A.; Niazmand, H.; Asadnia, M.; Razmjou, A.; Warkiani, M.E. Experimental and numerical study of elasto-inertial focusing in straight channels. *Biomicrofluidics* **2019**, *13*, 034103. [[CrossRef](#)] [[PubMed](#)]

13. Mukherjee, P.; Wang, X.; Zhou, J.; Papautsky, I. Single stream inertial focusing in low aspect-ratio triangular microchannels. *Lab Chip* **2018**, *19*, 147–157. [[CrossRef](#)] [[PubMed](#)]
14. Moloudi, R.; Oh, S.; Yang, C.; Warkiani, M.E.; Naing, M.W. Inertial particle focusing dynamics in a trapezoidal straight microchannel: Application to particle filtration. *Microfluid. Nanofluid.* **2018**, *22*, 33. [[CrossRef](#)]
15. Lee, D.-K.; Kwon, J.Y.; Cho, Y.H. Fabrication of microfluidic channels with various cross-sectional shapes using anisotropic etching of Si and self-alignment. *Appl. Phys. A Mater. Sci. Process.* **2019**, *125*, 291. [[CrossRef](#)]
16. Tirtaatmadja, V.; McKinley, G.; Cooper-White, J. Drop formation and breakup of low viscosity elastic fluids: Effects of molecular weight and concentration. *Phys. Fluids* **2006**, *18*, 043101. [[CrossRef](#)]
17. Lim, H.; Nam, J.; Shin, S. Lateral migration of particles suspended in viscoelastic fluids in a microchannel flow. *Microfluid. Nanofluid.* **2014**, *17*, 683–692. [[CrossRef](#)]
18. Kwon, J.-Y.; Kim, T.; Kim, J.; Cho, Y. Particle Focusing under Newtonian and Viscoelastic Flow in a Straight Rhombic Microchannel. *Micromachines* **2020**, *11*, 998. [[CrossRef](#)]
19. Lu, X.; Liu, C.; Hu, G.; Xuan, X. Particle manipulations in non-Newtonian microfluidics: A review. *J. Colloid Interface Sci.* **2017**, *500*, 182–201. [[CrossRef](#)]
20. Seo, K.W.; Kang, Y.J.; Lee, S.J. Lateral migration and focusing of microspheres in a microchannel flow of viscoelastic fluids. *Phys. Fluids* **2014**, *26*, 063301. [[CrossRef](#)]
21. Leshansky, A.M.; Bransky, A.; Korin, N.; Dinnar, U. Tunable Nonlinear Viscoelastic “Focusing” in a Microfluidic Device. *Phys. Rev. Lett.* **2007**, *98*, 234501. [[CrossRef](#)] [[PubMed](#)]
22. Kim, B.; Kim, J.M. Elasto-inertial particle focusing under the viscoelastic flow of DNA solution in a square channel. *Biomicrofluidics* **2016**, *10*, 024111. [[CrossRef](#)] [[PubMed](#)]
23. Asmolov, E.S. The inertial lift on a spherical particle in a plane Poiseuille flow at large channel Reynolds number. *J. Fluid Mech.* **1999**, *381*, 63–87. [[CrossRef](#)]